The effect of increasing model resolution on the Northern Hemisphere winter mid-latitude storm track: an equatorward shift due to contraction of the Hadley cell

Article

Published Version

Open Access

Lockwood, J., Athanasiadis, P., Baker, A. ORCID: https://orcid.org/0000-0003-2697-1350, Hodges, K. ORCID: https://orcid.org/0000-0003-0894-229X, Priestley, M., Roberts, M., Scaife, A., Vidale, P. L. ORCID: https://orcid.org/0000-0002-1800-8460 and Zappa, G. (2025) The effect of increasing model resolution on the Northern Hemisphere winter mid-latitude storm track: an equatorward shift due to contraction of the Hadley cell. Journal of Climate, 38 (17). pp. 4539-4551. ISSN 1520-0442 doi: 10.1175/JCLI-D-24-0414.1 Available at https://centaur.reading.ac.uk/122203/

To link to this article DOI: http://dx.doi.org/10.1175/JCLI-D-24-0414.1

Publisher: American Meteorological Society

The Effect of Increasing Model Resolution on the Northern Hemisphere Winter Midlatitude Storm Track: An Equatorward Shift due to Contraction of the Hadley Cell

JULIA F. LOCKWOOD,[a] PANOS J. ATHANASIADIS,[b] ALEXANDER J. BAKER,[c,d] KEVIN HODGES,[c,d]
MATTHEW D. K. PRIESTLEY,[e] MALCOLM ROBERTS,[a] ADAM A. SCAIFE,[a,e] PIER-LUIGI VIDALE,[c,d] AND
GIUSEPPE ZAPPA[f]

[a] *Met Office Hadley Centre, Exeter, United Kingdom*
[b] *Centro Euro-Mediterraneo sui Cambiamenti Climatici, Bologna, Italy*
[c] *National Centre for Atmospheric Science, Reading, United Kingdom*
[d] *Department of Meteorology, University of Reading, Reading, United Kingdom*
[e] *Department of Mathematics and Statistics, University of Exeter, Exeter, United Kingdom*
[f] *National Research Council of Italy, Institute of Atmospheric Sciences and Climate, Bologna, Italy*

(Manuscript received 12 August 2024, in final form 14 March 2025, accepted 31 March 2025)

ABSTRACT: We examine how changes in horizontal resolution impact the Northern Hemisphere winter midlatitude climatological storm-track position using the historical runs of six fully coupled climate models from the High-Resolution Model Intercomparison Project (HighResMIP). Each model has a low- and high-resolution version, with atmospheric resolutions from ~100–200 to ~25–50 km, respectively, and four of the six models also increase oceanic resolution from 1° to 0.25°. In all models, the storm-track position is more equatorward as resolution increases. This is associated with an intensification and narrowing of precipitation around the equator and a contraction of the Hadley cell. This shifts the subtropical jet equatorward, increasing the baroclinicity at lower latitudes, leading to more favorable conditions for storm genesis at these latitudes. The contraction of the Hadley cell with resolution is similar to that caused by El Niño on interannual time scales. Four of the six models, including those which increase atmospheric resolution only, show a corresponding El Niño–like sea surface temperature signature at high resolution. The Hadley cell contraction with resolution increase is not seen in models with prescribed sea surface temperatures. The increase in oceanic resolution drives the Hadley cell contraction in some models. In others, however, the increase in atmospheric resolution is the dominant driver, but only when the atmosphere is dynamically coupled with the ocean. These results show that increasing resolution alone could exacerbate the existing equatorward storm-track bias seen in CMIP6 models, although it is possible that this could be mitigated by optimization of parameterization settings.

KEYWORDS: Extratropical cyclones; Hadley circulation; Climate models

1. Introduction

The midlatitude storm track is a major component of the general circulation of Earth's atmosphere, with the storms (extratropical or midlatitude cyclones) being both driven by, and feeding back onto, the background westerly jets (Hoskins and Valdes 1990). In terms of impacts, winter storms bring extreme weather to midlatitudes and are the costliest natural hazard over Europe as measured by insured losses (Lockwood et al. 2022). Understanding storm-track climatology and how it may change in the future is also vital for water resource management: In large regions of the midlatitudes, extratropical cyclone associated precipitation makes up the majority of total precipitation, contributing up to 90% in some regions (Hawcroft et al. 2012). Previous studies have found that performance in historical simulations associated with model resolution can affect projections (Baker et al. 2019; Grist et al. 2021), therefore, it is important to accurately represent the midlatitude storm track in climate models to have confidence in future projections, as well as to understand current variability.

For the CMIP5 generation of models, Zappa et al. (2013) found that, for the North Atlantic sector, the model winter storm tracks were generally displaced equatorward or were too zonally oriented compared to reanalyses, although the higher-resolution models suffered less from these biases. For the Northern Hemisphere as a whole, Priestley et al. (2020) found that these biases persisted in CMIP6, albeit to a lesser extent, and again they found the biases reduced in higher-resolution models.

In this paper, we examine the Northern Hemisphere winter storm track in six models from the High-Resolution Model Intercomparison Project (HighResMIP; Haarsma et al. 2016). The HighResMIP models are the same generation as CMIP6, with each model having been run at a minimum of two different atmospheric resolutions: a low-resolution version with nominal grid spacing of ~ 100 km (comparable to a standard CMIP6 run) and a high-resolution version with nominal grid spacing of 25–50 km. Four of the six models studied also increase oceanic

---

Denotes content that is immediately available upon publication as open access.

Supplemental information related to this paper is available at the Journals Online website: https://doi.org/10.1175/JCLI-D-24-0414.s1.

Corresponding author: Julia Lockwood, julia.lockwood@metoffice.gov.uk

DOI: 10.1175/JCLI-D-24-0414.1

TABLE 1. Summary of models used in this study. Each model is run at LR and HR.

Model name	CNRM-CM6-1		EC-Earth3P		ECWMF-IFS			HadGEM3-GC3.1		CMCC-CM2		MPI-ESM1-2	
	LR	HR	LR	HR	LR	MR[a]	HR	LR	HR	LR	HR	LR	HR
Resolution name extension	LR	HR	LR	HR	LR	MR	HR	LL	HM	HR4	VHR4	HR	XR
Atmospheric grid spacing at 50°N (km)	142	50	71	36	50	50	25	135	25	64	18	67	34
Ocean grid[b]	ORCA1	ORCA025	ORCA1	ORCA025	ORCA1	ORCA025	ORCA025	ORCA1	ORCA025	ORCA025	ORCA025	TP04	TP04
Reference(s)	Voldoire et al. (2019)		Haarsma et al. (2020)		Roberts et al. (2018)			Roberts et al. (2019), Williams et al. (2018)		Cherchi et al. (2019)		Gutjahr et al. (2019)	

[a] For ECWMF-IFS, an additional "MR" simulation was run, which has an increase in oceanic resolution only.

[b] For the ocean grid, ORCA refers to the tripolar grid used by the NEMO ocean model, with ORCA1 and ORCA025 having approximately 1° and 0.25° grid spacings, respectively. TP04 refers to the tripolar grid of the MPIOM ocean model with 0.4° grid spacing.

resolution from 1° to 0.25° in their high-resolution versions. We focus on the results from the coupled, historical simulations, and use the atmosphere-only historical simulations to isolate the role of changes in atmospheric resolution only.

Generally, it is expected that model biases will reduce as resolution increases, due to improved representation of small-scale processes (e.g., Kirtman et al. 2012; Hodges et al. 2011). Studies assessing the HighResMIP experiment have found several improvements with increasing model resolution, including improved El Niño–Southern Oscillation (ENSO) simulations and ENSO teleconnections (Williams et al. 2024), and a reduction in some long-standing biases such as the double intertropical convergence zone (ITCZ; Moreno-Chamarro et al. 2022). For the models which increase oceanic resolution, a reduction of the cold sea surface temperature (SST) bias in the North Atlantic was found, leading to important benefits for blocking and for the realism of the jet's trimodality (Athanasiadis et al. 2022; Schiemann et al. 2020; Davini et al. 2021). In terms of extratropical cyclones, Priestley and Catto (2022) found improved representation of their structure and intensity, and Lockwood et al. (2022) found improvements in the number of potentially damaging storms reaching northern Europe. However, in some aspects, the high-resolution models show worse biases: For example, Moreno-Chamarro et al. (2022) found an increase in the equatorward bias of the annually averaged Northern Hemisphere subtropical jet in the high-resolution models. Baker et al. (2025, manuscript submitted to *J. Climate*) found a similar increase in subtropical jet bias when restricting the analysis to the North Atlantic sector for the winter season.

The aim of this paper is to investigate how the Northern Hemisphere winter [December–February (DJF)] storm-track position changes as model resolution is increased from ~100 to ~25 km, in the historical HighResMIP simulations. We find that the storm track intensifies on its equatorward side in the higher-resolution models, which is related to the more equatorward subtropical jet as identified in the previously mentioned studies, and in turn, we show that this is associated with changes in tropical precipitation and in the Hadley cell.

The paper is structured as follows: In section 2, we describe the data and methods used for the study. The results are presented in section 3, where we first show the changes in storm track and how they are similar to the changes in vertical wind shear (caused by the aforementioned shift in subtropical jet; section 3a). In section 3b, we examine changes in the zonal mean circulation and Hadley cell, and how they are related to changes in tropical precipitation. In section 3c, we discuss how these changes are related to sea surface temperatures and El Niño, and in section 3d, we discuss whether they are driven by changes in the atmospheric or oceanic resolution. Discussion and conclusions are given in section 4.

2. Data and methods

a. Model data

We evaluated the historical simulations from six different models from the CMIP6 HighResMIP (Haarsma et al. 2016), summarized in Table 1. All models contributed to the European Commission Horizon 2020–funded project, Process-based climate simulation: Advances in high-resolution modeling and European climate risk assessments (PRIMAVERA; primavera-h2020.eu). Each model was run at a minimum of two different horizontal atmospheric resolutions (with the vertical resolution remaining constant), but for this paper, we analyze only one representative "high" and "low" resolution (subsequently referred to as "LR" and "HR") for each model (see Table 1). One ensemble member was evaluated for each resolution.

The focus of the paper is the "hist-1950" simulations, which are fully coupled integrations with observed anthropogenic and natural forcings for the period 1950–2014. As shown in Table 1, four of the six models increase their oceanic resolution from 1° to 0.25° in their high-resolution versions, but two models (CMCC-CM2 and MPI-ESM1-2) keep their oceanic resolution constant.

To investigate the effect of increasing oceanic resolution only, in section 3d, we analyze an additional hist-1950 simulation, ECMWF-IFS-MR (Roberts et al. 2018). This model has the same atmospheric resolution as ECMWF-IFS-LR, but the oceanic resolution of ECMWF-IFS-HR (Table 1).

For comparison, we also analyze the atmosphere-only "highresSST-present" simulations, also for the period 1950–2014, in which the lower boundary is forced by the daily 1/4° Hadley Centre Sea Ice and Sea Surface Temperature dataset (HadISST.2.2.0; Kennedy et al. 2017). The highresSST-present simulations were run at the same atmospheric resolutions as for hist-1950.

As part of the HighResMIP protocol, for a clean evaluation of the impact of horizontal resolution, minimal retuning was applied when increasing resolution (Haarsma et al. 2016). Parameters that were changed are summarized in Roberts et al. (2020).

b. *Observational and reanalysis data*

As the high-resolution versions of each model have not been optimized by retuning, the aim of this paper is to identify the changes in storm track with resolution rather than comparison with observations. Nevertheless, for interest, we do compare with observations/reanalysis to investigate changes in model bias. For all variables, we use the ERA5 reanalysis (Hersbach et al. 2020) as the "observations," which has a horizontal spectral resolution of TL639 in the atmosphere (grid spacing of 31 km at 50° latitude). The ERA5 data were extracted for the time period common with the models (1950/51–2013/14), although ERA5 storm tracks were only available for the period 1979/80–2017/18 at the time of writing. In addition, for precipitation data, we verify against the Global Precipitation Climatology Project (GPCP; Adler et al. 2018) dataset, which is available from 1979 onward with a resolution of 2.5° latitude × 2.5° longitude (grid spacing ~ 280 km × 180 km at 50° latitude).

c. *Tracks*

The identification and tracking of cyclones in the model data are performed following the approach used in Hoskins and Hodges (2002) based on the Hodges (1995, 1999) tracking algorithm (TRACK). The cyclones are tracked on the 6-hourly, T42 spectrally filtered 850-hPa relative vorticity field. Planetary waves with a wavenumber less than 5 are filtered out to remove the large-scale background and improve reliability of the algorithm. The choice of spatial scale and season tracked (DJF) ensures cyclones are extratropical rather than tropical in nature. Only mobile cyclones with a maximum intensity greater than 1.0×10^{-5} s^{-1} lasting at least 2 days and traveling more than 1000 km in total are retained.

Track densities (number of cyclones per month per 5° spherical cap) are computed using the spherical kernel estimators described in Hodges (1996).

d. *Meridional streamfunction*

The mass weighted meridional streamfunction (Oort and Yienger 1996) at pressure level p and latitude ϕ, $\psi(\phi, p)$, is used to quantify the meridional overturning circulation cells (Hadley cell, Ferrel cell):

$$\psi(\phi, p) = \frac{2\pi a \cos\phi}{g}\int_0^p [v(\phi, p')]dp'.$$

Here, $[v(\phi, p)]$ is the zonal mean meridional wind at latitude ϕ and pressure p, a is the radius of the Earth, and g is the standard gravity. The integral is calculated numerically from the output at 19 pressure levels from 1000 to 100 hPa. To avoid artificial meridional mass flux at the lower boundary, the integral was performed from the top boundary (100 hPa) downward and its negative was taken.

e. *Track, wind shear, and precipitation indices*

To measure changes in the latitudinal position of the storm track and vertical wind shear (see section 3a), we define the following indices:

- Track position index = zonal mean track density averaged over 45°–55°N minus zonal mean track density over 30°–40°N.
- Wind shear index = zonal mean vertical wind shear over 40°–55°N minus zonal mean wind shear over 20°–35°N. The vertical wind shear is defined as the zonal wind at 250 hPa minus that at 850 hPa (U250–U850).

In both cases, a more positive index indicates a more northerly position in maximum track density or vertical wind shear. Note the slightly different latitudes used to define each index, which is discussed in section 3a.

To measure the "narrowing" of tropical precipitation around the equator, we define a tropical precipitation index as the zonal mean precipitation averaged over 7°–15°N minus zonal mean precipitation over 5°S–5°N (see section 3b). A more negative index indicates an increase of precipitation on the equator relative to north of the equator.

In all three indices defined above, the zonal means are taken over all longitudes, although we also briefly discuss the results when taking the zonal means over the North Pacific (longitudes 120°–240°E) and North Atlantic (longitudes 75°W–0°) sectors only.

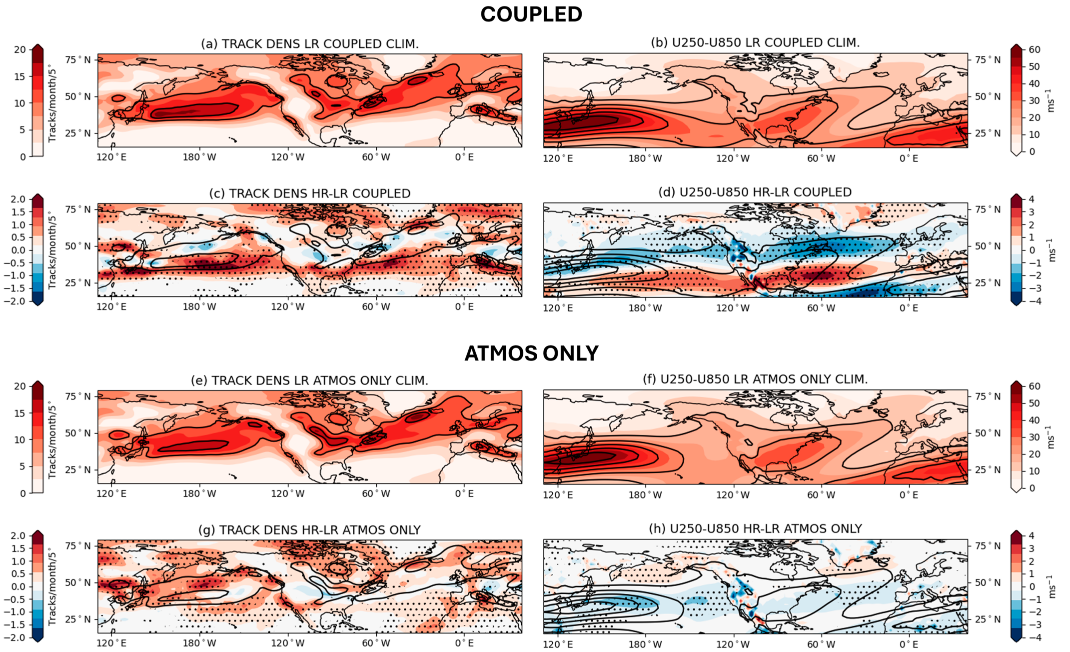

FIG. 1. The equatorward shift of track density and wind shear in high-resolution coupled models. (a) The climatological multimodel mean track density for the low-resolution coupled (hist-1950) models; (c) the multimodel mean difference in climatological track density between the high- and low-resolution coupled models. The contours show the climatological track density for the low-resolution models, with levels 10, 15, and 20 tracks per month per 5° spherical cap. (e),(g) As in (a) and (c), but for the atmosphere-only (highresSST-present) models; (b),(d),(f),(h) as in (a), (c), (e), and (g), but for vertical wind shear (U250–U850), with contours showing the climatological wind shear for the low-resolution models with levels starting at 15 m s^{-1} and increasing in 10 m s^{-1} increments. Stippling shows where at least five of the six models agree on the sign of the HR–LR change.

3. Results

All results presented below are for the Northern Hemisphere winter (DJF).

a. Storm track and vertical wind shear position

Figure 1a shows the climatological mean (1950–2014) Northern Hemisphere winter track density for the low-resolution coupled models. The difference between the high- and low-resolution coupled models (HR–LR) is shown in Fig. 1c. There is a general increase in track density with resolution, but superimposed is a clear strengthening of the track density on the equatorward side of the storm track in the high-resolution models. The increase in track density seen in this region is substantial, corresponding to a ~30%–40% increase in the Atlantic and a ~20% increase in the Pacific. There is high model agreement indicated by the stippling, which shows where at least five of the six models agree on the sign of the change (the HR–LR change for individual models is shown in Figs. S3–S8 in the online supplemental material). A similar equatorward shift in storm track is also seen if the storm track is defined by 2–6-day bandpass-filtered mean sea level pressure (e.g., Brayshaw et al. 2009), an Eulerian rather than Lagrangian measure of the storm track (not shown). Note, however, that Fig. S1 shows that relative to ERA5, the HR coupled models have an *increase* in equatorward storm-track bias compared to the LR models.

To investigate the cause of the equatorward track intensification, we consider the Eady growth rate, which is the maximum growth rate of baroclinic instability in the atmosphere (e.g., Charney 1947; Eady 1949), and it is these instabilities that contribute to the formation of midlatitude storms. The Eady growth rate is proportional to the product of the vertical wind shear and inverse of the static stability. Changes to the static stability were found to be small (not shown), but this is not the case for the wind shear: Figs. 1b and 1d show the LR mean and HR–LR difference, respectively, in climatological vertical wind shear of the zonal wind between 250 and 850 hPa (U250–U850) (HR–LR changes for individual models are shown in Figs. S3–S8). An equatorward shift of wind shear is seen, with high model agreement, mirroring the changes seen in the storm track. As with the storm track, there is an increase in equatorward bias of wind shear (Fig. S2). The changes in the full Eady growth rate (not shown) strongly resemble the changes in wind shear, in accordance with the wind shear being the dominant factor.

For comparison, the equivalent plots for the atmosphere-only runs are shown in the lower four panels of Fig. 1. Both the storm-track and wind shear changes are smaller in the atmosphere-only runs compared to the coupled runs, and the strong signal for the equatorward shift is not seen. On the contrary, in the Pacific in particular, there appears to be a poleward shift of the storm track and wind shear. A poleward shift as the resolution is increased was also seen in the atmosphere-only aquaplanet simulations of Lu et al. (2015).

To quantify the equatorward shift in storm track and wind shear in each model, we calculate the track position and wind shear indices as defined in section 2e. The latitude bands used to define the track position index are further north than those for the wind shear index because the storm-track response appears to be further north (Figs. 1c,d). This is consistent with the fact that cyclones travel poleward (Tamarin-Brodsky and Kaspi 2017), and cyclone centers tend to be poleward of the region of maximum baroclinicity (Hoskins and Valdes 1990). To verify that changes in storm track and wind shear at these latitudes are indeed related, we look at the *interannual* data from each model. We linearly regress the seasonal (DJF) track density anomalies at each grid point onto the seasonal zonal mean wind shear index anomalies for the coupled runs [so the linear regression is performed on approximately 770 data points at each grid point (64 years × 6 models × 2 resolutions for each model)]. The track and wind shear index anomalies are taken with respect to the climatology of each particular resolution model run to take into account systematic differences between the runs. The filled contours in Fig. 2a show the change in track density estimated from this linear regression for a change in wind shear index of -1.76 m s^{-1}, the measured HR–LR multimodel mean change. The maximum changes in track density for the interannual data lie poleward of the bands used to define the wind shear index (shown in gray in Fig. 2a). Notably, the regions of increased track density lie at very similar latitudes to those in Fig. 1c, showing that the HR–LR changes in wind shear and track density are internally consistent.

The track position index against wind shear index for each model is shown in Fig. 2b (one point for each of the coupled and atmosphere-only, high- and low-resolution runs). There is a positive correlation ($r = 0.54$) between the track position and wind shear indices across all model runs. For *all* the coupled models (filled symbols), the high-resolution versions (stars) show a decrease in track and wind shear indices compared to the low-resolution versions (circles), indicating an equatorward displacement. In general, the atmosphere-only runs (empty symbols) have smaller changes in track and wind shear indices between resolutions, consistent with the results in Fig. 1. The result holds when considering the Pacific and Atlantic basins separately, with correlations between the track and wind shear indices of 0.61 and 0.70 in each basin, respectively.

The CMCC coupled model shows a markedly smaller decrease in wind shear index between resolutions compared to the other models. Inspection of the respective spatial map of HR–LR wind shear (Fig. S7b) shows that CMCC does show an equatorward shift in wind shear over the east Pacific and Atlantic, but it is partially offset by a poleward shift in the west Pacific.

Overall, the consistency between changes in the storm track and wind shear in both the coupled and atmosphere-only models indicates that the wind shear and storm-track changes are clearly related. The question then remains as to what drives the equatorward shift in vertical wind shear? The zonal nature of the response, and the fact that the largest changes in storm track and wind shear lie at subtropical latitudes, point to a connection with the Hadley cell. We investigate this further in the following section.

(a) Regr(track density, wind shear index)
INTERANNUAL

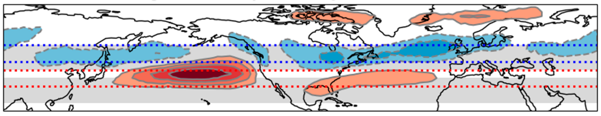

(b) Track density index vs wind shear index

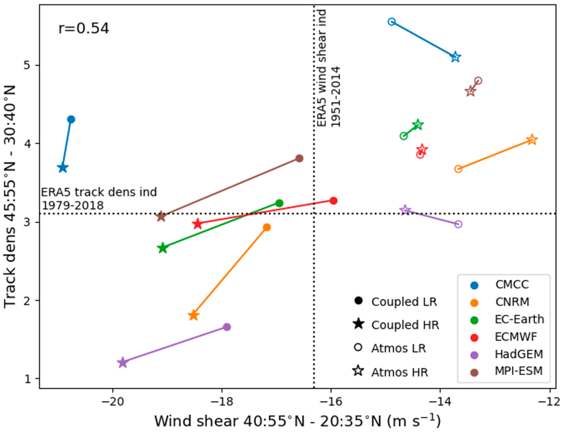

FIG. 2. Relationship between track density and vertical wind shear: (a) Regression of track density at each grid point onto the zonal wind shear index, calculated on the coupled model interannual data (filled contours; levels -0.25, -0.5 cyclones per month per 5° spherical cap in blue and 0.25, 0.5, 0.75, 1.0 cyclones per month per 5° spherical cap in red). The gray bands show the latitudes used to calculate the wind shear index, and the blue and red dotted lines show the latitudes used to calculate the track density index. (b) Scatterplot of track density index against wind shear index (climatological values) across all models (coupled and atmosphere only, and low and high resolution). The dotted lines mark the observed values.

b. *Zonal mean circulation and the Hadley cell*

To measure changes in the zonal mean circulation and the Hadley cell, in Fig. 3, we plot, throughout the troposphere, the HR–LR change in zonal mean zonal wind, meridional streamfunction (ψ), zonal mean vertical velocity in pressure coordinates (ω), as well as zonal mean precipitation. For the coupled models, Fig. 3a shows an equatorward shift of the subtropical jet with increasing resolution (which gives rise to the equatorward shift in vertical wind shear), with strong interhemispheric symmetry. Accompanied with this, Fig. 3b shows a narrowing of the northern branch of the Hadley cell, with enhanced upward motion around the equator but reduced either side of it (Fig. 3c). The changes in precipitation (Fig. 3d) reflect the changes in vertical velocity, with regions of enhanced precipitation associated with regions of enhanced upward motion. Similar, but smaller, differences are seen in the annual means of these quantities. There is strong agreement

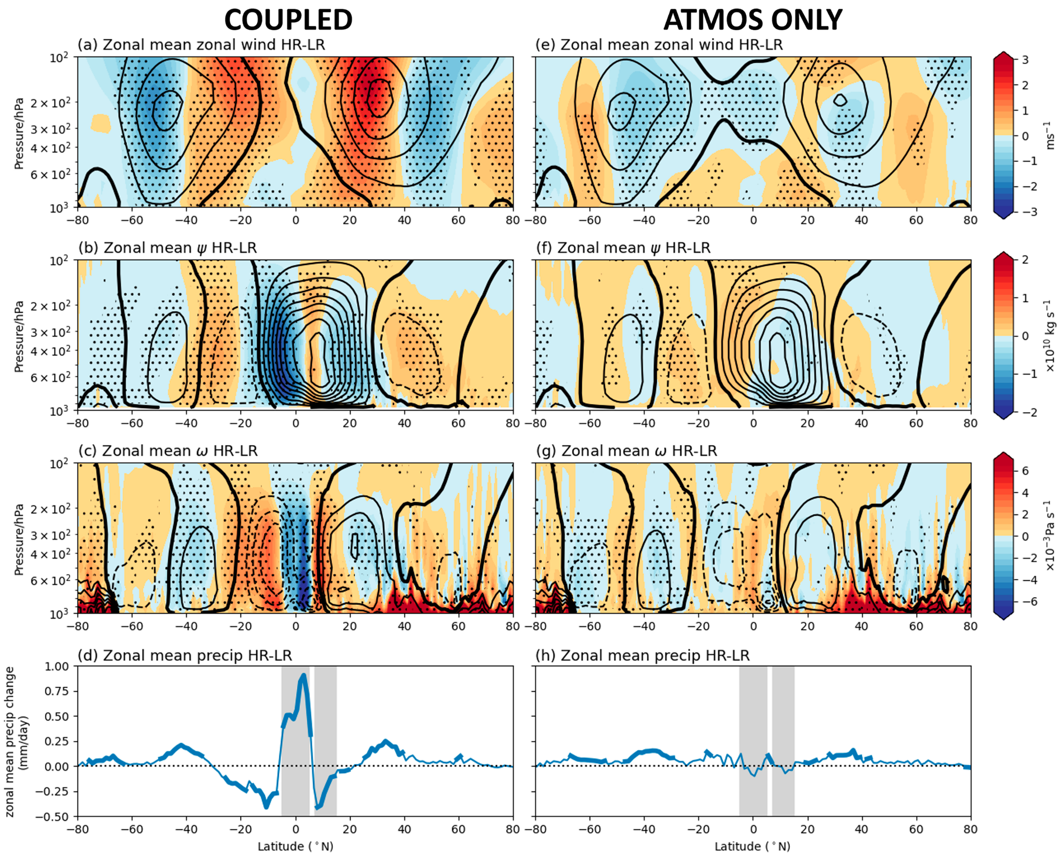

FIG. 3. Changes to the Hadley cell: (a) Mean HR–LR change in zonal mean zonal wind for the coupled models (colors) and LR climatology (contours in steps of 5 $\mathrm{m\,s^{-1}}$); (b) as in (a), but for zonal mean meridional streamfunction, ψ (LR climatology contour steps are 2.5×10^{10} kg $\mathrm{s^{-1}}$); (c) as in (a), but for vertical velocity in pressure coordinates, ω (negative indicates upward motion; LR climatology contour steps are 0.01 Pa $\mathrm{s^{-1}}$). In (a)–(c), the zero contour for the LR climatology is marked with a thick black line, and stippling marks where at least 5/6 models agree on the sign of the HR–LR difference; (d) HR–LR change in zonal mean precipitation for the coupled models. The thick line marks where at least 5/6 models agree on the sign of the HR–LR difference, and the gray bands mark the latitudes used to calculate the tropical precipitation index. (e)–(h) As in (a)–(d), but for the atmosphere-only models.

between models, shown by the stippling. In contrast, the atmosphere-only models show small changes and little model agreement in these measures (Figs. 3e–h). Equivalent plots for individual models are shown in Figs. S3–S8.

The almost exact correspondence in the coupled models between the HR–LR precipitation and vertical velocity changes shows they are undoubtedly related, but are the changes in tropical precipitation related to the Hadley cell and zonal wind changes? To investigate this, we examine the relationship between tropical precipitation and zonal mean wind and meridional streamfunction in the *interannual* model data.

We first calculate the tropical precipitation index defined in section 2e (the latitudes used to define the index are marked by the gray shading in Fig. 3d). Using the interannual anomalies from each of the coupled model runs, we regress zonal wind and meridional streamfunction onto the precipitation index (using the same method as in section 3a for Fig. 2a). Figure 4 compares the measured multimodel mean HR–LR change in zonal wind and meridional streamfunction, with that estimated from the interannual linear regression (using a change in tropical precipitation index of −0.86 mm $\mathrm{day^{-1}}$, the measured HR–LR value).

The interannual responses to the change in tropical precipitation index are strikingly similar to the HR–LR differences. This adds weight to the hypothesis that the intensifying and narrowing of equatorial precipitation as resolution is increased are related to the intensification and contraction of the Hadley cell, drawing the subtropical jet and storm track equatorward. One notable difference in the interannual response is that the strengthening of the Hadley cell between 0° and 10°N is more pronounced. This could be because the precipitation index used to quantify the HR–LR changes in tropical precipitation does not capture all the relevant information; zonal asymmetries could be important, for example.

The relationship between tropical precipitation and storm-track position can be seen across models, as demonstrated in Fig. 5. This shows a scatterplot of the track position index against the tropical precipitation index for each model run

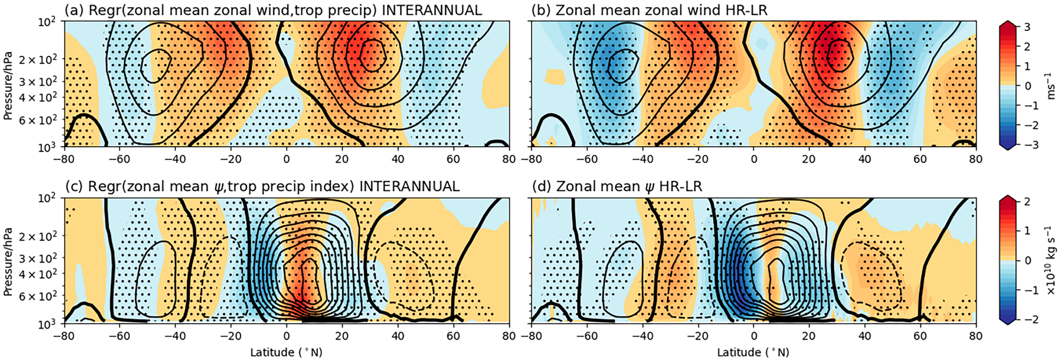

FIG. 4. Response to increasing resolution resembles interannual variability in the Hadley cell: Regression of (a) zonal mean zonal wind and (c) zonal mean meridional streamfunction onto the tropical precipitation index, calculated on the coupled model interannual data. The values shown are those estimated for a change in tropical precipitation index of -0.86 mm day^{-1}, the measured HR–LR value. Contours show the LR climatology (levels as in Fig. 3), and stippling shows where the regression coefficient is statistically significant at the 95% confidence level. The HR–LR changes are shown in (b) and (d) for comparison (as in Figs. 3a,b, with stippling marking model agreement).

(coupled and atmosphere only, high and low resolution), showing a positive relationship between the two measures ($r = 0.63$). *All* of the coupled models (filled symbols) have a decrease in tropical precipitation index (i.e., narrowing of equatorial precipitation) as they increase resolution, along with the equatorward shift in storm track.

When considering each basin separately, for the Pacific, the correlation between tropical precipitation and track indices remains high ($r = 0.51$), but it falls to 0.17 over the Atlantic. We argue that the Atlantic storm-track shift is still likely related to the tropical precipitation changes since previous studies have shown that Pacific variability, such as that associated with El Niño, is known to impact subtropical jet strength and storm track in the Atlantic (e.g., Seager et al. 2003). The relationship between the precipitation index and El Niño is discussed further in the next section.

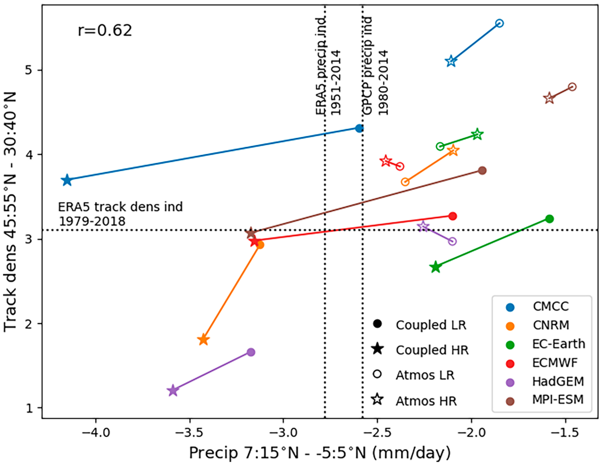

FIG. 5. Relationship between tropical precipitation and track density: Scatterplot of climatological track density index against tropical precipitation index across all models (coupled and atmosphere only; and low and high resolution). Dotted lines mark the observed values. For the precipitation index, two observed estimates are shown, from ERA5 (1950/51–2013/14) and GPCP (1979/80–2013/14).

c. *Connection with tropical surface temperatures and El Niño*

It is well established that on interannual time scales, narrow tropical heating, in particular that caused by El Niño, leads to the intensification and contraction of the Hadley cell, accompanied by an equatorward shift in subtropical jet and storm track (e.g., Seager et al. 2003; Lu et al. 2008; Graff and LaCasce 2012; Tandon et al. 2013; Qiu et al. 2023). Indeed, El Niño is very strongly related to the tropical precipitation index defined above: Using the interannual data from the coupled models, the correlation between the anomalies in precipitation index and El Niño (measured by the Niño-3.4 index: SST anomalies in the region 5°S–5°N, 170°–120°W) is $r = -0.9$.

In Fig. 6a, we plot the HR–LR multimodel mean change in surface temperature for the coupled models. An El Niño–like temperature pattern can indeed be seen in the higher-resolution models. To see how this change affects the model bias, in Fig. 6b, we plot the difference between observed and LR multimodel mean surface temperature; in locations where Figs. 6a and 6b are identical, the increase in resolution has fully mitigated the biases at low resolution. Comparing Figs. 6a and 6b, we see that the El Niño–like temperature pattern in the high-resolution models offsets (and overshoots) a small cold bias in the equatorial Pacific.

Figure 6c shows the HR–LR change in tropical precipitation, and the difference between observations and the LR models is shown in Fig. 6d. Comparison of Figs. 6c and 6d shows that the HR models mitigate many of the precipitation biases in the LR models, including the equatorial dry bias in the Pacific (cf. Williams et al. 2024).

The interannual precipitation response to El Niño is plotted in Fig. 6e. Here, to quantify the interannual response, rather than performing linear regression as before, we select from the ~770 years' of data the years for which the Niño-3.4 SST anomaly is close to the measured HR–LR value (+0.73 K,

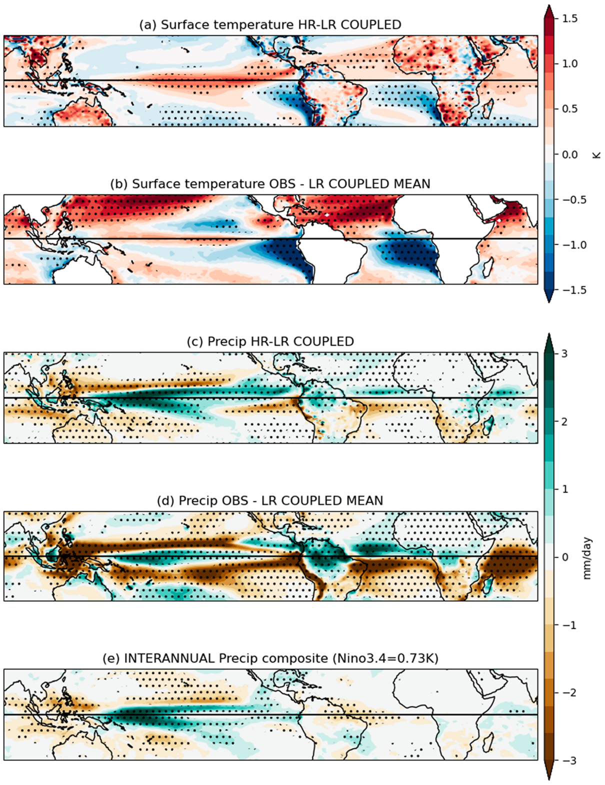

FIG. 6. The relationship between El Niño and tropical precipitation: (a) HR–LR change in surface temperature for the coupled models; (b) observed (ERA5) surface temperature minus LR coupled model mean (plotted for sea points only); (c),(d) as in (a) and (b), but for precipitation (observations are GPCP); and (e) composite showing the precipitation anomaly associated with a Niño-3.4 anomaly of +0.73 K (the measured HR–LR value) in the interannual coupled model data (see text for details). In (a)–(d), stippling shows where at least 5/6 models agree on the sign of the change (either HR–LR, or observations–LR). In (e), stippling shows where the composite is significantly different from zero at the 95% confidence level.

with a tolerance of ±0.1 K; giving 42 data points), and calculate the mean of precipitation anomaly for these years. Linear regression is inappropriate in this case because Niño-3.4 anomalies can lead to zero precipitation in certain regions in the models, resulting in a highly nonlinearly response. Comparing Fig. 6e to Fig. 6c shows that the HR–LR change in precipitation strongly resembles the interannual response to El Niño in the Pacific.

There is strong model agreement in the sign of the HR–LR changes in Niño-3.4 SSTs and tropical precipitation. However, inspection of the maps of HR–LR surface temperature for the individual models reveals that two models, CNRM-CM6 and EC-Earth3P, show very little change in their equatorial Pacific (Niño-3.4) temperatures (Figs. S3d and S4d). Despite their lack of change in equatorial Pacific temperatures, they still show an El Niño–like precipitation change in their high-resolution version, albeit somewhat smaller in magnitude compared to the other models (Figs. S3c and S4c).

In Fig. 7, we show scatterplots of the interannual precipitation index against Niño-3.4 (absolute) temperatures for the HR and LR simulations of the individual coupled models, along with histograms comparing the distributions of interannual precipitation index and Niño-3.4 temperatures. For both CNRM-CM6 and EC-Earth3P (top row), there is a small yet clear shift to a more negative precipitation index in the HR models, independent of Niño-3.4 temperatures (i.e., for a given Niño-3.4 temperature, the distribution of precipitation indices is more negative in the HR models compared to the LR ones). For these two models, in Fig. S9, we have also plotted the wind shear index (section 2e) against the precipitation index. Figure S9 shows that the shift to more negative wind shear indices in the HR is consistent with the shift in precipitation indices, despite there being virtually no change in Niño-3.4 temperatures.

This behavior is in stark contrast to the ECMWF-IFS and MPI-ESM1-2 models, where there is a clear shift to more positive Niño-3.4 temperatures in the HR models which can fully explain the decrease in precipitation index. For the remaining two models (CMCC-CM2 and HadGEM3), the shift to more negative precipitation index with increasing resolution appears to be caused by a combination of both the Niño-3.4 temperatures and an independent driver. We note that for HadGEM3, this independent driver acts against the Niño-3.4 changes, leading to a more *positive* precipitation index for a given Niño-3.4 temperature in the HR model. Figure 7 also reveals diverse changes to El Niño variability as resolution increases between each model. For example, CNRM-CM6 and MPI-ESM1-2 show a marked decrease in the range of Niño-3.4 temperatures at higher resolution, whereas ECMWF-IFS shows an increase.

To summarize, all six models show an El Niño–like precipitation pattern as they increase resolution, but only four of the six models show the corresponding El Niño signature in climatological mean SST.

d. Are the changes caused by the increase in atmospheric or oceanic resolution?

Two of the models analyzed in this study increase only the atmospheric resolution: MPI-ESM1-2 and CMCC-CM2. Note that these are *not* the models which did not show an increase in Niño-3.4 temperatures with resolution; on the contrary, both of these models show clear El Niño–like signatures in the SSTs of their high-resolution versions (Figs. S7d and S8d). This would imply that in these cases, the *atmospheric* resolution causes the shift to a more El Niño–like state, leading to the contraction of the Hadley cell and more equatorward storm track.

Changes to El Niño with resolution for the MPI-ESM1-2 suite of models, including the ones analyzed in this paper, were studied by Arora (2023). They also found an increase in SSTs in the Niño-3.4 region in MPI-ESM1-2-XR (referred to as the HR model in this paper) compared to the lower-resolution models, and this was associated with an increased interannual amplitude of the intraseasonal zonal wind in the equatorial Pacific. Lin et al. (2023) found that, for atmosphere-only simulations of a single model, increasing resolution led to

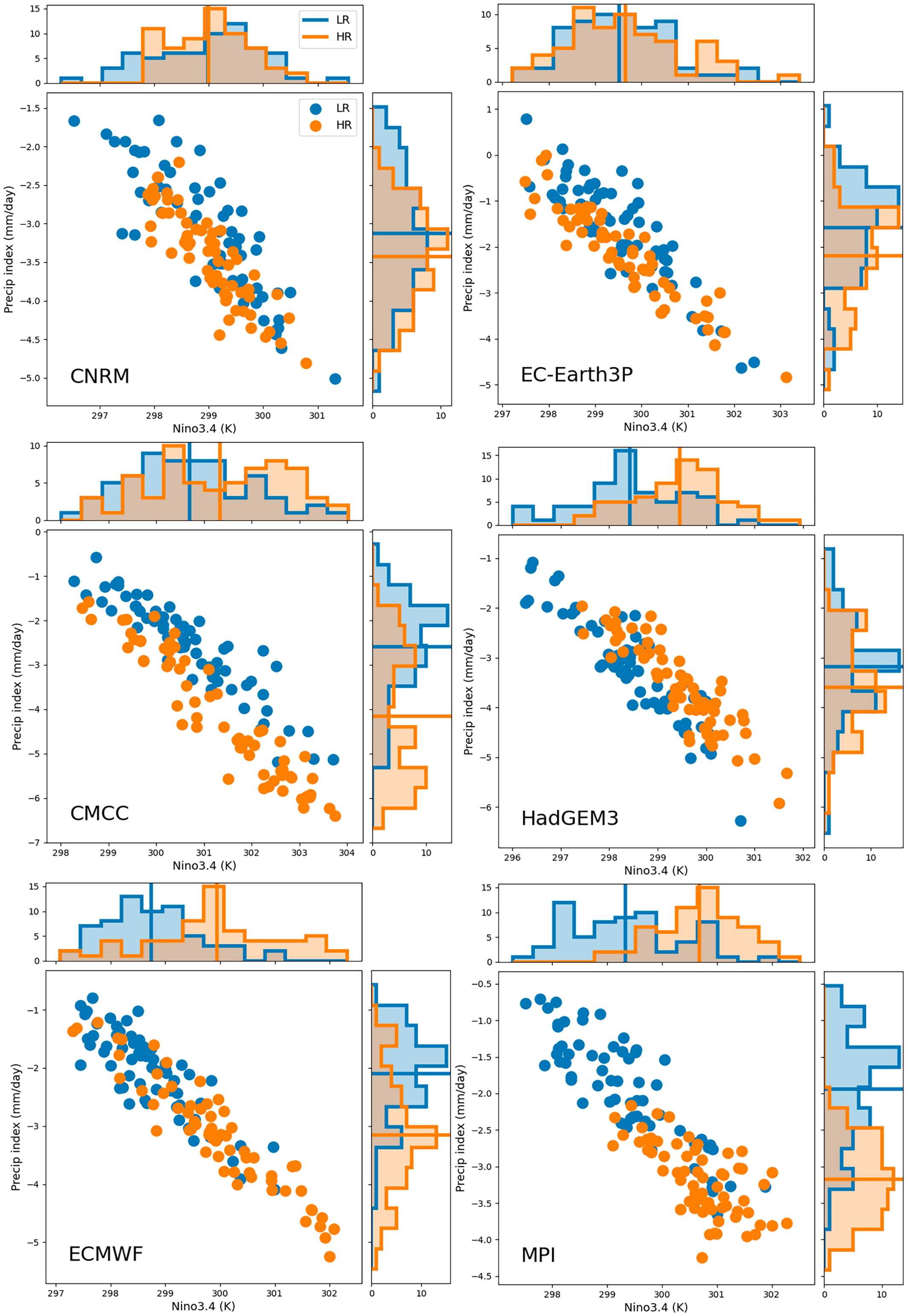

FIG. 7. A driver independent of Niño-3.4 temperatures causing the changes in precipitation index in some models: Scatterplot of precipitation index against absolute Niño-3.4 temperatures in the LR (blue) and HR (orange) coupled simulations. The histograms along the *x* and *y* axes show the distribution of Niño-3.4 temperatures and precipitation indices in the LR (blue) and HR (orange) simulations, and the vertical lines show the climatological means.

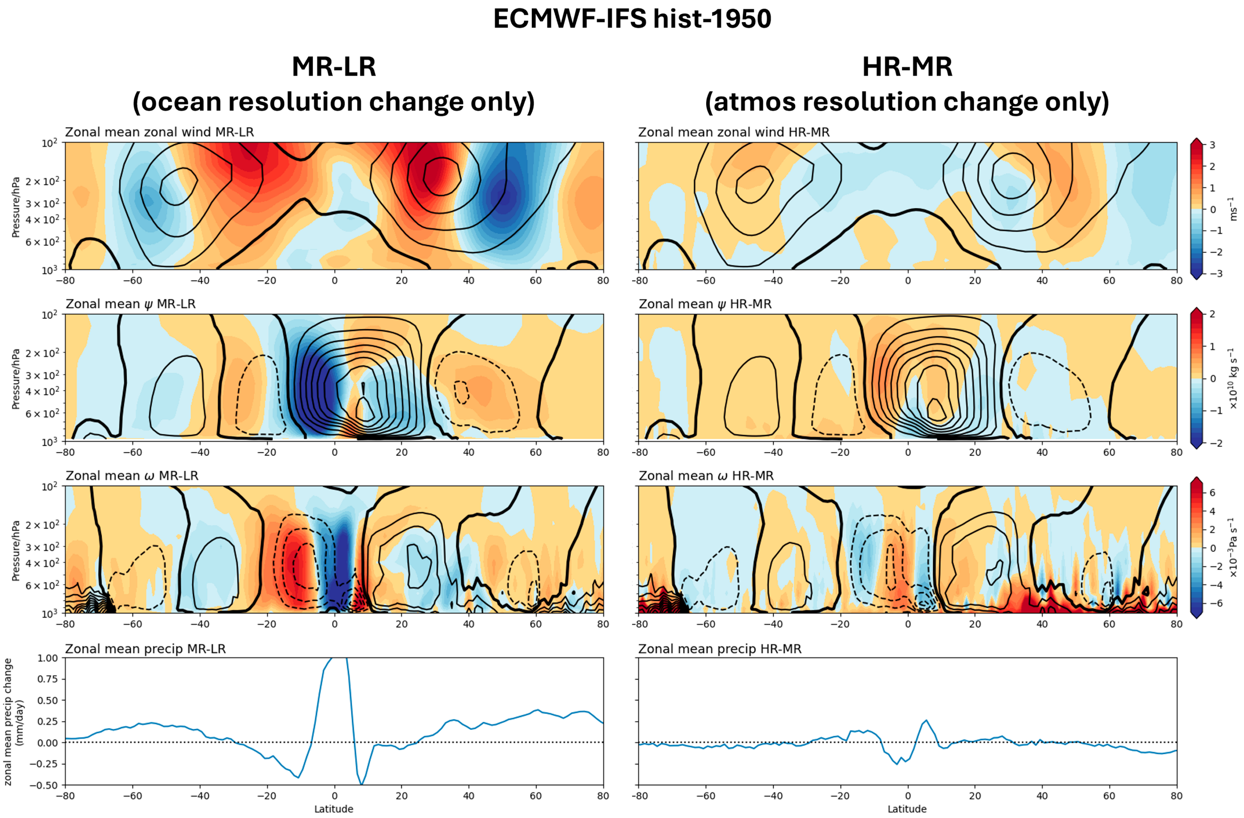

FIG. 8. Changes to the Hadley cell are driven by the change in oceanic resolution for ECMWF-IFS: Panels as in Fig. 3, but for the ECMWF-IFS model only. (left) ECMWF-IFS-MR–ECMWF-IFS-LR, showing the effect of increasing oceanic resolution only; (right) ECMWF-IFS-HR–ECMWF-IFS-MR, showing the effect of increasing atmospheric resolution only.

enhanced organized convection in the tropics, which could also lead to changes in equatorial zonal winds. One hypothesis is that the changes to the equatorial winds and their variability are driven by the change in atmospheric resolution, but only in the coupled models can these changes interact with the ocean to produce the SST and tropical precipitation anomalies, amplifying the initial atmospheric change and causing the contraction of the Hadley cell. It has been suggested that for the EC-Earth3P model, the ocean–atmosphere coupling strength in the tropical Pacific decreases in the high-resolution version (Haarsma et al. 2020), which could explain why in this model El Niño–like precipitation changes are observed without the associated SSTs as resolution is increased.

Alternatively, it could be that changes to the extratropics drive the Hadley cell contraction: The improved representation of extratropical cyclone structure and intensity found in these same models (Priestley and Catto 2022) could lead to increased eddy fluxes of momentum, mass, and moisture which decrease Hadley cell width (Davis and Birner 2019; Freisen et al. 2022).

Further testing is necessary to confirm the role of atmospheric processes and ocean–atmosphere coupling; for example, running the simulations with a slab ocean configuration could demonstrate the role of ocean–atmosphere coupling in amplifying tropical convection changes as atmospheric resolution is increased.

To test the impact of increasing *oceanic* resolution only, we have analyzed the ECMWF-IFS-MR simulation (see Table 1). This model has the same atmospheric resolution as ECMWF-IFS-LR (~50 km at midlatitudes) but the oceanic resolution of ECMWF-IFS-HR (ORCA025). The changes to the Hadley cell between the MR and LR (ocean resolution only increasing) and HR and MR (atmospheric resolution only increasing) are shown in Fig. 8. The MR–LR differences resemble those of the coupled multimodel mean HR–LR differences in Fig. 3 and are almost identical to the HR–LR changes for ECMWF-IFS shown S5. Thus, in contrast to the MPI-ESM1-2 and CMCC-CM2 models, for ECMWF-IFS, the contraction of the Hadley cell occurs when the *oceanic* resolution is increased, and increasing the atmospheric resolution has a much smaller impact.

Roberts et al. (2018) also noted the increased equatorial temperatures in the Pacific in the -MR model compared to the -LR one, and attributed this to better resolved oceanic meridional eddy heat transport. Similar changes in meridional eddy heat transport are seen in HadGEM3-GC3.1 between the HM and LL versions (Roberts et al. 2019), implying a similar mechanism could be operating here.

It therefore appears that the increases in *both* atmospheric and oceanic resolution are playing a role in shifting the high-resolution models toward a more El Niño–like state, and that the primary cause is different for each model.

4. Discussion and conclusions

In this paper, we have shown that as model horizontal resolution is increased from ~100 to ~25–50 km, coupled models show a more equatorward Northern Hemisphere winter storm track. This is associated with an intensification and narrowing of precipitation on the equator and contraction of the Hadley cell. This shifts the subtropical jet equatorward, increasing the baroclinicity at lower latitudes, leading to more favorable conditions for extratropical storm genesis and development at these latitudes. The changes in tropical precipitation and contraction of the Hadley cell with resolution are similar to those caused by El Niño on interannual time scales. These responses appear remarkably robust across all coupled models, albeit to varying degrees. Four of the six models, including those which increase atmospheric resolution *only*, show a corresponding El Niño–like sea surface temperature signature at high resolution. The Hadley cell contraction with resolution increase is not seen in models with prescribed sea surface temperatures. We have shown the increase in oceanic resolution drives the Hadley cell contraction in the ECMWF-IFS model, and presumably others such as HadGEM3-GC3.1. However, in other models, for example, MPI-ESM1-2, the increase in atmospheric resolution drives the Hadley cell contraction, but only when the atmosphere is dynamically coupled with the ocean.

The contraction of the Hadley cell describes well the changes in the storm track with resolution to first order, but there are many other possible impacts of increasing model resolution which could explain some of the model diversity in changes of track density seen in Figs. S3–S8. For example, using the same models, Athanasiadis et al. (2022) showed that the North Atlantic cold bias is substantially reduced in the models with increased oceanic resolution, leading to changes in baroclinicity and Eady growth rate in this region. Priestley et al. (2023) linked the equatorward bias of the North Pacific and North Atlantic storm tracks to a cold bias in central North Pacific SSTs. Inspection of Figs. 6b and 6c shows that, on average, the SST bias in the central North Pacific worsens in the high-resolution models, although there is little model agreement. It is of course difficult to disentangle whether this is driven by oceanic processes or a response to the changes in the Hadley cell or other atmospheric changes.

In addition to surface effects, processes at the tropopause and stratosphere could also modify the storm track: For example, changes in gravity wave drag at the tropopause caused by changes in orography, or sensitivity of the gravity wave parameterization to resolution, could alter the planetary wave patterns that steer the storm track (Pithan et al. 2016), as well as the position of the subtropical jet (Eichinger et al. 2020) and its associated baroclinicity.

Finally, we note that, while it is robust, the equatorward shift in storm track as model resolution increases appears to exacerbate the existing equatorward bias. Although there is an inconsistency in the time periods compared between the models and reanalysis, the fact that wind shear also increases its equatorward bias corroborates this result.

Introducing more realistic representations of physical processes can often lead to increases in bias during model development, but further rounds of development focusing on optimization of parameterization schemes and settings could mitigate these biases. For example, several studies have shown different convection schemes can lead to changes in the mean state of the equatorial Pacific and El Niño variability (Zhu et al. 2017), and also the strength of the Hadley cell (Bhattacharya et al. 2018), while Eichinger et al. (2020) showed the sensitivity of the subtropical jet to parameterized orographic gravity waves, all of which could in turn affect the position of the storm track.

We note that while the existing storm-track biases are exacerbated with an increase in resolution, it does not necessarily imply the lower-resolution models are more trustworthy for projections, as there is sometimes a weak relationship between projections and mean state biases (Scaife et al. 2019). However, until better tuned and improved high-resolution simulations become available, expectedly in CMIP7, we advise users not to *exclusively* use the high-resolution models in this paper to study storm-track and jet projections and the associated uncertainty.

Acknowledgments. This research has been supported by the European Commission, Horizon 2020 [PRIMAVERA (Grant 641727)] and IS-ENES3 (Grant 824084). JFL would like to thank Stephen Hardiman and Martin Andrews for helpful discussions on possible causes of the equatorward shift. MR was supported by the Met Office Hadley Centre Climate Programme funded by DSIT. The authors thank three anonymous referees whose comments led to considerable improvements to this work.

Data availability statement. All raw PRIMAVERA model data are available from https://esgf-index1.ceda.ac.uk/projects/esgf-ceda. ERA5 reanalysis data are available from https://cds.climate.copernicus.eu/#!/home. GPCP precipitation data are available from https://psl.noaa.gov/data/gridded/data.gpcp.html.

REFERENCES

Adler, R. F., and Coauthors, 2018: The Global Precipitation Climatology Project (GPCP) monthly analysis (new version 2.3) and a review of 2017 global precipitation. *Atmosphere*, **9**, 138, https://doi.org/10.3390/atmos9040138.

Arora, A., 2023: Revisiting the effect of increasing horizontal resolution on the evolution of El Niño in a coupled model. *Global Planet. Change*, **230**, 104256, https://doi.org/10.1016/j.gloplacha.2023.104256.

Athanasiadis, P. J., and Coauthors, 2022: Mitigating climate biases in the midlatitude North Atlantic by increasing model resolution: SST gradients and their relation to blocking and the jet. *J. Climate*, **35**, 6985–7006, https://doi.org/10.1175/JCLI-D-21-0515.1.

Baker, A. J., and Coauthors, 2019: Enhanced climate change response of wintertime North Atlantic circulation, cyclonic activity, and precipitation in a 25-km-resolution global atmospheric model. *J. Climate*, **32**, 7763–7781, https://doi.org/10.1175/JCLI-D-19-0054.1.

Bhattacharya, R., S. Bordoni, K. Suselj, and J. Teixeira, 2018: Parameterization interactions in global aquaplanet simulations.

J. Adv. Model. Earth Syst., **10**, 403–420, https://doi.org/10.1002/2017MS000991.

Brayshaw, D. J., T. Woollings, and M. Vellinga, 2009: Tropical and extratropical responses of the North Atlantic atmospheric circulation to a sustained weakening of the MOC. *J. Climate*, **22**, 3146–3155, https://doi.org/10.1175/2008JCLI2594.1.

Charney, J. G., 1947: The dynamics of long waves in a baroclinic westerly current. *J. Meteor.*, **4**, 136–162, https://doi.org/10.1175/1520-0469(1947)004<0136:TDOLWI>2.0.CO;2.

Cherchi, A., and Coauthors, 2019: Global mean climate and main patterns of variability in the CMCC-CM2 coupled model. *J. Adv. Model. Earth Syst.*, **11**, 185–209, https://doi.org/10.1029/2018MS001369.

Davini, P., A. Weisheimer, M. Balmaseda, S. J. Johnson, F. Molteni, C. D. Roberts, R. Senan, and T. N. Stockdale, 2021: The representation of winter Northern Hemisphere atmospheric blocking in ECMWF seasonal prediction systems. *Quart. J. Roy. Meteor. Soc.*, **147**, 1344–1363, https://doi.org/10.1002/qj.3974.

Davis, N. A., and T. Birner, 2019: Eddy influences on the Hadley circulation. *J. Adv. Model. Earth Syst.*, **11**, 1563–1581, https://doi.org/10.1029/2018MS001554.

Eady, E. T., 1949: Long waves and cyclone waves. *Tellus*, **1**, 33–52, https://doi.org/10.1111/j.2153-3490.1949.tb01265.x.

Eichinger, R., H. Garny, P. Šácha, J. Danker, S. Dietmüller, and S. Oberländer-Hayn, 2020: Effects of missing gravity waves on stratospheric dynamics; Part 1: Climatology. *Climate Dyn.*, **54**, 3165–3183, https://doi.org/10.1007/s00382-020-05166-w.

Freisen, P. F., J. M. Arblaster, C. Jakob, and J. M. Rodríguez, 2022: Investigating tropical versus extratropical influences on the Southern Hemisphere tropical edge in the unified model. *J. Geophys. Res. Atmos.*, **127**, e2021JD036106, https://doi.org/10.1029/2021JD036106.

Graff, L. S., and J. H. LaCasce, 2012: Changes in the extratropical storm tracks in response to changes in SST in an AGCM. *J. Climate*, **25**, 1854–1870, https://doi.org/10.1175/JCLI-D-11-00174.1.

Grist, J. P., S. A. Josey, B. Sinha, J. L. Catto, M. J. Roberts, and A. C. Coward, 2021: Future evolution of an eddy rich ocean associated with enhanced East Atlantic storminess in a coupled model projection. *Geophys. Res. Lett.*, **48**, e2021GL092719, https://doi.org/10.1029/2021GL092719.

Gutjahr, O., D. Putrasahan, K. Lohmann, J. H. Jungclaus, J.-S. von Storch, N. Brüggemann, H. Haak, and A. Stössel, 2019: Max Planck Institute Earth System Model (MPI-ESM1.2) for the High-Resolution Model Intercomparison Project (HighResMIP). *Geosci. Model Dev.*, **12**, 3241–3281, https://doi.org/10.5194/gmd-12-3241-2019.

Haarsma, R., and Coauthors, 2020: HighResMIP versions of EC-Earth: EC-Earth3P and EC-Earth3P-HR—Description, model computational performance and basic validation. *Geosci. Model Dev.*, **13**, 3507–3527, https://doi.org/10.5194/gmd-13-3507-2020.

Haarsma, R. J., and Coauthors, 2016: High Resolution Model Intercomparison Project (HighResMIP v1.0) for CMIP6. *Geosci. Model Dev.*, **9**, 4185–4208, https://doi.org/10.5194/gmd-9-4185-2016.

Hawcroft, M. K., L. C. Shaffrey, K. I. Hodges, and H. F. Dacre, 2012: How much Northern Hemisphere precipitation is associated with extratropical cyclones? *Geophys. Res. Lett.*, **39**, L24809, https://doi.org/10.1029/2012GL053866.

Hersbach, H., and Coauthors, 2020: The ERA5 global reanalysis. *Quart. J. Roy. Meteor. Soc.*, **146**, 1999–2049, https://doi.org/10.1002/qj.3803.

Hodges, K. I., 1995: Feature tracking on the unit sphere. *Mon. Wea. Rev.*, **123**, 3458–3465, https://doi.org/10.1175/1520-0493(1995)123<3458:FTOTUS>2.0.CO;2.

——, 1996: Spherical nonparametric estimators applied to the UGAMP model integration for AMIP. *Mon. Wea. Rev.*, **124**, 2914–2932, https://doi.org/10.1175/1520-0493(1996)124<2914:SNEATT>2.0.CO;2.

——, 1999: Adaptive constraints for feature tracking. *Mon. Wea. Rev.*, **127**, 1362–1373, https://doi.org/10.1175/1520-0493(1999)127<1362:ACFFT>2.0.CO;2.

——, R. W. Lee, and L. Bengtsson, 2011: A comparison of extratropical cyclones in recent reanalyses ERA-Interim, NASA MERRA, NCEP CFSR, and JRA-25. *J. Climate*, **24**, 4888–4906, https://doi.org/10.1175/2011JCLI4097.1.

Hoskins, B. J., and P. J. Valdes, 1990: On the existence of storm-tracks. *J. Atmos. Sci.*, **47**, 1854–1864, https://doi.org/10.1175/1520-0469(1990)047<1854:OTEOST>2.0.CO;2.

——, and K. I. Hodges, 2002: New perspectives on the Northern Hemisphere winter storm tracks. *J. Atmos. Sci.*, **59**, 1041–1061, https://doi.org/10.1175/1520-0469(2002)059<1041:NPOTNH>2.0.CO;2.

Kennedy, J., H. Titchner, N. Rayner, and M. Roberts, 2017: input4MIPs.MOHC.SSTsAndSeaIce.HighResMIP.MOHC-HadISST-2-2-0-0-0, version 20170505. Earth System Grid Federation, https://doi.org/10.22033/ESGF/input4MIPs.1221.

Kirtman, B. P., and Coauthors, 2012: Impact of ocean model resolution on CCSM climate simulations. *Climate Dyn.*, **39**, 1303–1328, https://doi.org/10.1007/s00382-012-1500-3.

Lin, P., Y. Ming, and T. Robinson, 2023: On the resolution sensitivity of equatorial precipitation in a GFDL global atmospheric model. *J. Adv. Model. Earth Syst.*, **15**, e2022MS003300, https://doi.org/10.1029/2022MS003300.

Lockwood, J. F., G. S. Guentchev, A. Alabaster, S. J. Brown, E. J. Palin, M. J. Roberts, and H. E. Thornton, 2022: Using high-resolution global climate models from the PRIMAVERA project to create a European winter windstorm event set. *Nat. Hazards Earth Syst. Sci.*, **22**, 3585–3606, https://doi.org/10.5194/nhess-22-3585-2022.

Lu, J., G. Chen, and D. M. W. Frierson, 2008: Response of the zonal mean atmospheric circulation to El Niño versus global warming. *J. Climate*, **21**, 5835–5851, https://doi.org/10.1175/2008JCLI2200.1.

——, ——, L. R. Leung, D. A. Burrows, Q. Yang, K. Sakaguchi, and S. Hagos, 2015: Toward the dynamical convergence on the jet stream in aquaplanet AGCMs. *J. Climate*, **28**, 6763–6782, https://doi.org/10.1175/JCLI-D-14-00761.1.

Moreno-Chamarro, E., and Coauthors, 2022: Impact of increased resolution on long-standing biases in HighResMIP-PRIMAVERA climate models. *Geosci. Model Dev.*, **15**, 269–289, https://doi.org/10.5194/gmd-15-269-2022.

Oort, A. H., and J. J. Yienger, 1996: Observed interannual variability in the Hadley circulation and its connection to ENSO. *J. Climate*, **9**, 2751–2767, https://doi.org/10.1175/1520-0442(1996)009<2751:OIVITH>2.0.CO;2.

Pithan, F., T. G. Shepherd, G. Zappa, and I. Sandu, 2016: Climate model biases in jet streams, blocking and storm tracks resulting from missing orographic drag. *Geophys. Res. Lett.*, **43**, 7231–7240, https://doi.org/10.1002/2016GL069551.

Priestley, M. D. K., and J. L. Catto, 2022: Improved representation of extratropical cyclone structure in HighResMIP models. *Geophys. Res. Lett.*, **49**, e2021GL096708, https://doi.org/10.1029/2021GL096708.

——, D. Ackerley, J. L. Catto, K. I. Hodges, R. E. McDonald, and R. W. Lee, 2020: An overview of the extratropical storm tracks in CMIP6 historical simulations. *J. Climate*, **33**, 6315–6343, https://doi.org/10.1175/JCLI-D-19-0928.1.

——, ——, ——, and ——, 2023: Drivers of biases in the CMIP6 extratropical storm tracks. Part I: Northern Hemisphere. *J. Climate*, **36**, 1451–1467, https://doi.org/10.1175/JCLI-D-20-0976.1.

Qiu, W., M. Collins, and A. A. Scaife, 2023: Winter subtropical highs, the Hadley circulation and baroclinic instability. *J. Geophys. Res. Atmos.*, **128**, e2023JD039604, https://doi.org/10.1029/2023JD039604.

Roberts, C. D., R. Senan, F. Molteni, S. Boussetta, M. Mayer, and S. P. E. Keeley, 2018: Climate model configurations of the ECMWF Integrated Forecasting System (ECMWF-IFS cycle 43r1) for HighResMIP. *Geosci. Model Dev.*, **11**, 3681–3712, https://doi.org/10.5194/gmd-11-3681-2018.

Roberts, M. J., and Coauthors, 2019: Description of the resolution hierarchy of the global coupled HadGEM3-GC3.1 model as used in CMIP6 HighResMIP experiments. *Geosci. Model Dev.*, **12**, 4999–5028, https://doi.org/10.5194/gmd-12-4999-2019.

——, and Coauthors, 2020: Impact of model resolution on tropical cyclone simulation using the HighResMIP–PRIMAVERA multimodel ensemble. *J. Climate*, **33**, 2557–2583, https://doi.org/10.1175/JCLI-D-19-0639.1.

Scaife, A. A., and Coauthors, 2019: Tropical rainfall predictions from multiple seasonal forecast systems. *Int. J. Climatol.*, **39**, 974–988, https://doi.org/10.1002/joc.5855.

Schiemann, R., and Coauthors, 2020: Northern Hemisphere blocking simulation in current climate models: Evaluating progress from the Climate Model Intercomparison Project Phase 5 to 6 and sensitivity to resolution. *Wea. Climate Dyn.*, **1**, 277–292, https://doi.org/10.5194/wcd-1-277-2020.

Seager, R., N. Harnik, Y. Kushnir, W. Robinson, and J. Miller, 2003: Mechanisms of hemispherically symmetric climate variability. *J. Climate*, **16**, 2960–2978, https://doi.org/10.1175/1520-0442(2003)016<2960:MOHSCV>2.0.CO;2.

Tamarin-Brodsky, T., and Y. Kaspi, 2017: Enhanced poleward propagation of storms under climate change. *Nat. Geosci.*, **10**, 908–913, https://doi.org/10.1038/s41561-017-0001-8.

Tandon, N. F., E. P. Gerber, A. H. Sobel, and L. M. Polvani, 2013: Understanding Hadley Cell expansion versus contraction: Insights from simplified models and implications for recent observations. *J. Climate*, **26**, 4304–4321, https://doi.org/10.1175/JCLI-D-12-00598.1.

Voldoire, A., and Coauthors, 2019: Evaluation of CMIP6 DECK experiments with CNRM-CM6-1. *J. Adv. Model. Earth Syst.*, **11**, 2177–2213, https://doi.org/10.1029/2019MS001683.

Williams, K. D., and Coauthors, 2018: The Met Office Global Coupled Model 3.0 and 3.1 (GC3.0 and GC3.1) configurations. *J. Adv. Model. Earth Syst.*, **10**, 357–380, https://doi.org/10.1002/2017MS001115.

Williams, N. C., A. A. Scaife, and J. A. Screen, 2024: Effect of increased ocean resolution on model errors in El Niño–Southern Oscillation and its teleconnections. *Quart. J. Roy. Meteor. Soc.*, **150**, 1489–1500, https://doi.org/10.1002/qj.4655.

Zappa, G., L. C. Shaffrey, K. I. Hodges, P. G. Sansom, and D. B. Stephenson, 2013: A multimodel assessment of future projections of North Atlantic and European extratropical cyclones in the CMIP5 climate models. *J. Climate*, **26**, 5846–5862, https://doi.org/10.1175/JCLI-D-12-00573.1.

Zhu, J., A. Kumar, W. Wang, Z.-Z. Hu, B. Huang, and M. A. Balmaseda, 2017: Importance of convective parameterization in ENSO predictions. *Geophys. Res. Lett.*, **44**, 6334–6342, https://doi.org/10.1002/2017GL073669.